

# Proximity-Effect-Induced Superconductivity in Nb/Sb<sub>2</sub>Te<sub>3</sub>-Nanoribbon/Nb Junctions

Jinzhong Zhang, Abdur Rehman Jalil, Pok-Lam Tse, Jonas Kölzer, Daniel Rosenbach, Helen Valencia, Martina Luysberg, Martin Mikulics, Gregory Panaitov, Detlev Grützmacher, Zhigao Hu, Jia Grace Lu, and Thomas Schäpers\*

**Nanohybrid superconducting junctions using antimony telluride (Sb<sub>2</sub>Te<sub>3</sub>) topological insulator nanoribbons and Nb superconducting electrodes are fabricated using electron beam lithography and magnetron sputtering. The effects of bias current, temperature, and magnetic field on the transport properties of the junctions in a four-terminal measurement configuration are investigated. Two features are observed. First, the formation of a Josephson weak-link junction. The junction is formed by proximity-induced areas in the nanoribbon right underneath the inner Nb electrodes which are connected by the few tens of nanometers short Sb<sub>2</sub>Te<sub>3</sub> bridge. At 0.5 K a critical current of 0.15  $\mu$ A is observed. The decrease of the supercurrent with temperature is explained in the framework of a diffusive junction. Furthermore, the Josephson supercurrent is found to decrease monotonously with the magnetic field indicating that the structure is in the small-junction limit. As a second feature, a transition is also observed in the differential resistance at larger bias currents and larger magnetic fields, which is attributed to the suppression of the proximity-induced superconductive state in the nanoribbon area underneath the Nb electrodes.**

(TIs).<sup>[1–5]</sup> Such 3D TI materials have an insulating energy gap in the bulk and gapless edge or surface states on the sample boundary. They are protected by time-reversal-symmetry, which is well explained by a single spin-momentum-locked Rashba-Dirac cone. From a practical point of view, TIs can be applied in nanoelectronic and spintronic devices since back-scattering in the charge transport is prohibited, i.e. the propagation direction of surface electrons is robustly locked to the spin orientation.<sup>[4–7]</sup> Among the 3D TIs mentioned above, Sb<sub>2</sub>Te<sub>3</sub> is particularly interesting since it comprises a relatively large bulk band gap of about 200 meV and a Dirac point within the gap.<sup>[1,8]</sup> Regarding phenomena at low temperatures Zhang *et al.* reported pressure-induced superconductivity in a Bi<sub>2</sub>Te<sub>3</sub> single crystal with a critical temperature  $T_c \sim 3$  K.<sup>[9]</sup> A superconducting state in the topologically protected

surface states can also be gained by coupling to a conventional metallic superconductor,<sup>[10–16]</sup> high- $T_c$  superconductors,<sup>[17]</sup> or iron-based superconductors.<sup>[18]</sup> It was predicted that topological

## 1. Introduction

It is well-known that the binary compounds Bi<sub>2</sub>Te<sub>3</sub>, Bi<sub>2</sub>Se<sub>3</sub>, and Sb<sub>2</sub>Te<sub>3</sub> belong in the new material class of topological insulators


Dr. J. Zhang, A. R. Jalil, J. Kölzer, D. Rosenbach, Dr. M. Mikulics, Prof. D. Grützmacher, Prof. T. Schäpers  
Peter Grünberg Institut (PGI-9)  
Forschungszentrum Jülich  
52425 Jülich, Germany  
E-mail: th.schapers@fz-juelich.de

Dr. J. Zhang, A. R. Jalil, J. Kölzer, D. Rosenbach, Dr. M. Mikulics, Prof. D. Grützmacher, Prof. T. Schäpers  
JARA-Fundamentals of Future Information Technology  
Jülich-Aachen Research Alliance  
Forschungszentrum Jülich and RWTH Aachen University  
52425 Jülich, Germany

Dr. J. Zhang, Prof. Z. Hu  
Technical Center for Multifunctional Magneto-Optical Spectroscopy (Shanghai)  
Engineering Research Center of Nanophotonics & Advanced Instrument (Ministry of Education)  
Department of Materials  
School of Physics and Electronics Science  
East China Normal University  
Shanghai 200241, China

P.-L. Tse, Prof. J. G. Lu  
Department of Physics and Astronomy and Department of Electrophysics  
University of Southern California  
Los Angeles CA, 90089, USA  
H. Valencia, Dr. M. Luysberg  
Ernst Ruska Center  
Forschungszentrum Jülich  
52425 Jülich, Germany

Dr. G. Panaitov  
Institute of Complex Systems (ICS-8)  
Forschungszentrum Jülich  
52425 Jülich, Germany

 The ORCID identification number(s) for the author(s) of this article can be found under <https://doi.org/10.1002/andp.202000273>

© 2020 The Authors. Published by WILEY-VCH Verlag GmbH & Co. KGaA, Weinheim. This is an open access article under the terms of the Creative Commons Attribution License, which permits use, distribution and reproduction in any medium, provided the original work is properly cited.

DOI: 10.1002/andp.202000273

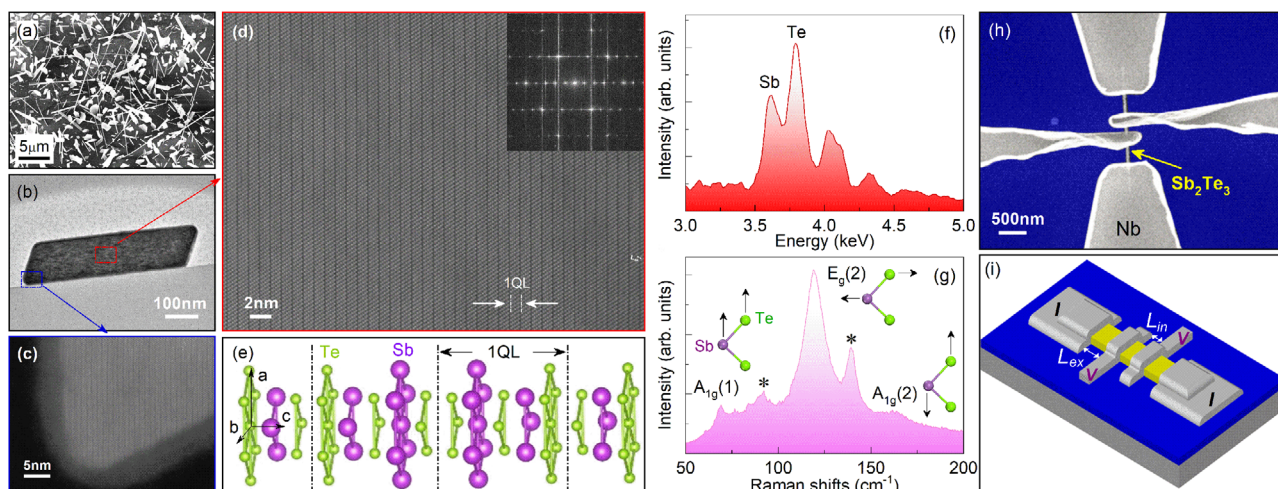


**Figure 1.** (Color online) a) Scanning electron micrograph (SEM) of the as-grown  $\text{Sb}_2\text{Te}_3$  nanoribbons on a  $\text{Si}/\text{SiO}_2$  substrate. HRSTEM images (S=Scanning) of b) a cross section, c) corner and d) center areas as well as FFT (inset) of a single  $\text{Sb}_2\text{Te}_3$  NR. e) Crystal structure of the  $\text{Sb}_2\text{Te}_3$  topological insulator. A quintuple layer consists of five atomic  $\text{Te-Sb-Te-Sb-Te}$  layers. f) Energy dispersive X-ray spectroscopy and g) Raman spectra with mode assignments of a  $\text{Sb}_2\text{Te}_3$  single nanoribbon. The peaks marked with asterisks (\*) at 90 and  $140\text{ cm}^{-1}$  are assigned to the  $E_u(3)$  and  $A_{2u}(3)$  modes, respectively. h) SEM image of a  $\text{Sb}_2\text{Te}_3$  NR-based junction contacted with Nb superconducting electrodes and i) Schematic illustration of a four-terminal current driven measurement geometry.  $L_{\text{ex}}$  and  $L_{\text{in}}$  correspond to the distance between the outer and inner contacts and between the inner contacts, respectively.

insulators combined with superconducting electrodes can host Majorana zero modes.<sup>[19–22]</sup> Braiding these Majorana zero modes is the basis for topological quantum computation,<sup>[23,24]</sup> which is considered to be less prone to decoherence than other concepts. First evidence of the existence of Majorana zero modes in topological material based Josephson junctions have been reported already.<sup>[16,25–27]</sup> However, there still exist many challenges to realize topological Josephson junctions, therefore, clarifying the physical mechanism of proximity effect induced superconductivity in 3D TI materials is beneficial for advancing the field of topological quantum computing.

Experimentally, the TI binary compounds are often not truly insulating especially for bulk materials because of the high carrier concentration originating from intrinsic defects/impurities, which will mask the intrinsic topological surface electrical transport.<sup>[2,28,29]</sup> For example, major defects in  $\text{Sb}_2\text{Te}_3$  are  $\text{Sb}_{\text{Te}}$  antisite defects resulting in  $p$ -type charge carriers, while  $\text{Bi}_2\text{Te}_3$  exhibits  $n$ -type behavior due to Te vacancies acting as donors.<sup>[29,30]</sup> Fortunately, low-dimensional films, nanowires/nanoribbons and quantum dots offer a unique nanoscale platform to explore intrinsic surface states because of the high surface-to-bulk ratio and the effective Fermi level tuning. The band structure of 1D TI nanoribbons (NRs) is significantly modified since the confined surface electron states encircle the nanoribbon coherently leading to a gap closing and opening when an axial magnetic field is applied.<sup>[31,32]</sup> In magnetotransport the presence of these closed-loop states manifest themselves by the appearance of Aharonov–Bohm type oscillations.<sup>[33–38]</sup> Recently, we fabricated normal-metal-contacted  $\text{Au}/\text{Sb}_2\text{Te}_3\text{-NR}/\text{Au}$  devices and investigated the electrical band structure and quantum transport using a quasi four-terminal current driven measurement scheme.<sup>[38]</sup> Specifically, the topologically protected surface states in the intrinsic  $p$ -type  $\text{Sb}_2\text{Te}_3$  NRs were confirmed by nanoscale angle-resolved photoemission spectroscopy. The observed Aharonov–Bohm

oscillations were attributed to quantum transport effects of the topologically protected closed-loop surface states around the TI NRs. As mentioned above, Majorana zero modes are predicted to be present at the interface of a TI and an  $s$ -wave superconductor (SC). This motivated us to fabricate  $\text{Sb}_2\text{Te}_3$ -based nanoribbon devices with Nb superconducting contacts instead of normal metal electrodes. The superconducting proximity effects of the topological surface states have been investigated to tune the superconducting state in the  $\text{Sb}_2\text{Te}_3$  NRs by applying a magnetic field perpendicular to the Nb/ $\text{Sb}_2\text{Te}_3$ -NR/Nb junction plane.

## 2. Results and Discussion

### 2.1. Crystalline Structure and Microstructure Analysis

$\text{Sb}_2\text{Te}_3$  nanoribbons were synthesized by Au-catalyzed chemical vapor deposition in a tube furnace with Sb and Te powders.<sup>[38,39]</sup> The as-grown NRs on a  $\text{Si}/\text{SiO}_2$  substrate are shown in **Figure 1a**. For device fabrication the  $\text{Sb}_2\text{Te}_3$  NRs are transferred to a  $\text{Si}/\text{SiO}_2$  substrate, as depicted in the transmission electron microscopy image (cf. **Figure 1b**). **Figure 1c** reveals that there exists an about 5-nm-thick oxide layer on the NR surface. The high-resolution scanning transmission electron microscopy (HRSTEM) image of the cross section of a  $\text{Sb}_2\text{Te}_3$  NR shown in **Figure 1d** confirms that the crystalline quality is very high. For clarity, a schematic crystallographic structure of  $\text{Sb}_2\text{Te}_3$  is illustrated in **Figure 1e**. The crystal is stacked in so-called quintuple layers (QLs) with a thickness of about 1 nm along the  $c$ -axis direction in a  $\text{Te-Sb-Te-Sb-Te}$  sequence. The quintuple layers form a hexagonal packing structure in the  $a$ - $b$  plane. From **Figure 1d** we can conclude that the structural order degree of the quintuple layer is very high. The van der Waals gaps (dark stripes) separating the quintuple layers can be observed clearly. The corresponding fast Fourier

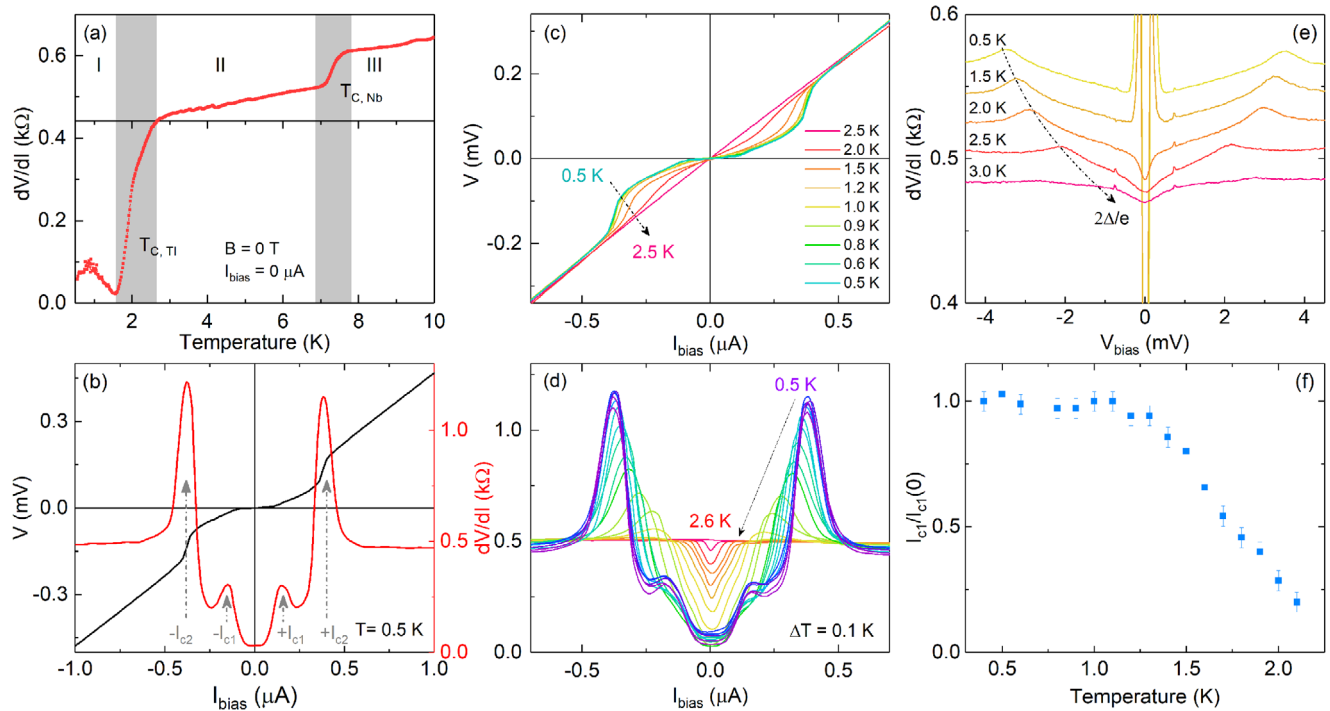


**Figure 2.** (Color online) a) Four-terminal current-driven measurements of  $dV/dI$  of a Nb/Sb<sub>2</sub>Te<sub>3</sub>-nanoribbon/Nb junction during cooling process. There are two transitions ( $T_{c,TI}$  and  $T_{c,Nb}$ ) labelled by vertical shadows, which are related to Sb<sub>2</sub>Te<sub>3</sub> nanoribbons and Nb leads, respectively. The finite signal below 2 K is attribute to the relative large excitation current. b)  $I$ - $V$  characteristics and corresponding  $dV/dI$  of a Sb<sub>2</sub>Te<sub>3</sub>-based junction at the temperature of 0.5 K. Two pairs of peaks are located at around  $\pm 0.15$  and  $\pm 0.38$   $\mu$ A. c)  $I$ - $V$  as a function bias current at temperatures between 0.5 and 2.5 K. d)  $dV/dI$  versus bias current at various temperatures. e)  $dV/dI$  versus bias voltage at various temperatures. Note that the curves are shifted vertically for clarity. The arrow indicates the peak position trend. f)  $I_{c1}/I_{c1}(0)$  as a function of temperature.

transform (FFT) is indexed, which confirms that the as-grown Sb<sub>2</sub>Te<sub>3</sub> NRs are single crystalline.

Figure 1f shows the energy dispersive X-ray spectroscopy (EDS) spectrum of a single ribbon, with the peaks assign to Sb and Te indicated. In addition, X-ray diffraction<sup>[38]</sup> and Raman spectra indicate that the as-grown Sb<sub>2</sub>Te<sub>3</sub> NRs have a rhombohedral geometry with a space group  $D_{3d}^5$  ( $R\bar{3}m$ ) at room temperature (cf. Figure 1g). There are three first-order Raman-active modes nearby 69, 119, and 163 cm<sup>-1</sup>, which are assigned to  $A_{1g}(1)$ ,  $E_g(2)$ , and  $A_{1g}(2)$ , respectively. Additionally, the corresponding symmetric vibrations at the  $\Gamma$ -point are illustrated. The  $A_{1g}$  modes involve lattice vibrations along the  $c$ -axis, while the  $E_g$  mode is related to vibrations in the  $a$ - $b$  plane.<sup>[40]</sup> Note that the appearance of infrared-active modes ( $E_u(3)$  and  $A_{2u}(3)$ ) marked with asterisks (\*) in the Raman spectrum might be related to symmetry breaking, for example, by surface band bending, or by quantum size effects in 1D Sb<sub>2</sub>Te<sub>3</sub> nanoribbons.<sup>[41–44]</sup>

Figure 1h shows an Sb<sub>2</sub>Te<sub>3</sub> NR-based junction device, which is fabricated using electron beam lithography and magnetron sputtering. The width ( $W$ ) of the NR is about 75 nm. The separations of external-internal ( $L_{ex}$ ) and internal-internal ( $L_{in}$ ) Nb electrodes are around 500 and 90 nm, respectively (cf. Figure 1i). The inner contact fingers have a width of 250 nm. The outer superconducting Nb leads are employed to apply a direct current ( $I_{bias}$ ) or/and an alternating current ( $I_{AC}$ ), while the inner pair of contacts serve as voltage probes, as displayed in Figure 1i.<sup>[45,46]</sup> The electrical transport behavior of the TI-based nanodevices is

investigated with the aid of a <sup>3</sup>He cryostat down to a temperature of 0.4 K.

## 2.2. Temperature Dependence of the Superconductivity in Nb/Sb<sub>2</sub>Te<sub>3</sub>-NR/Nb Junctions

Figure 2a shows the temperature dependence of the differential resistance ( $dV/dI$ ) measured in a four-terminal configuration using an AC current of 40 nA at zero magnetic field. The measurements reveal that the Nb electrodes have a transition between the superconducting and normal state at around  $T_{c,Nb} \approx 6.5$  K. From the relation of the electron-phonon coupling strength  $2\Delta/k_B T_{c,Nb} \approx 3.9$ , with  $k_B$  the Boltzmann constant and inserting  $T_{c,Nb}$  we estimate a Nb energy gap  $\Delta$  of 1.4 meV at  $T = 0$ .<sup>[47]</sup> Because of the proximity to the topological insulator there might be some deviation from the cited  $\Delta/T_{c,Nb}$  ratio. At about 1.5 K we observe another drop of  $dV/dI$  which we assign to the transition temperature  $T_{c,TI}$  of the Nb/Sb<sub>2</sub>Te<sub>3</sub>-NR/Nb junction. It means that the junction has a proximity induced superconducting state at low temperature. The two-step feature has been observed before in normal metal or semiconductor-based Josephson junctions, for example, Nb/Au/Nb<sup>[48]</sup> or PbIn/PbS/PbIn junctions.<sup>[49]</sup> The normal state four-terminal resistance ( $R_N$ ) of the present Nb/Sb<sub>2</sub>Te<sub>3</sub>-NR/Nb junction is about 650  $\Omega$  at temperatures above  $T_{c,Nb}$ .

The superconducting behavior is confirmed by the current-voltage ( $I$ - $V$ ) characteristics and the corresponding differential resistance ( $dV/dI$ ) at 0.5 K, as shown in Figure 2b. At low temperatures, the value of  $dV/dI$  at zero bias current is almost zero. As the bias current ( $I_{\text{bias}}$ ) increases,  $dV/dI$  increases slowly and then reaches the first peaks at around  $\pm 0.15 \mu\text{A}$ , followed by sharp peaks at approximately  $\pm 0.38 \mu\text{A}$ . As outlined in more detail below, we attribute these features to superconducting transitions at critical currents  $I_{c1}$  and  $I_{c2}$  to the junction itself and to proximity induced areas in the TI below the Nb electrodes, respectively. However, at the current stage it is not possible to discriminate between a supercurrent flowing in the surface states or in the bulk of the nanoribbon. In order to further investigate the superconducting behavior of the TI-based nanodevice, the  $I$ - $V$  characteristics and the corresponding  $dV/dI$  curves are recorded at various temperatures, as shown in Figures 2c and d, respectively. As the temperature increases from 0.5 K, it was found that the superconducting plateau disappears at around 1.4 K close to  $T_{c,\text{TI}}$  while the  $I$ - $V$  curve becomes linear at 2.5 K (see also Figure S1, Supporting Information). This is in accordance with the results derived from the temperature dependent differential resistance shown in Figure 2a.

Figure 2e shows  $dV/dI$  in a large bias voltage range at various temperatures. One finds a pair of distinct peaks with corresponding position of the left peak indicated by an arrow. At  $T = 0.5$  K the peaks are located at about  $\pm 3.4$  meV. They can be assigned to the onset of Andreev reflection at  $2\Delta$ .<sup>[50,51]</sup> The reason, that the peaks are found at higher energies compared to the previously obtained value of  $2\Delta = 2.8$  meV extracted from  $T_{c,\text{Nb}}$  can be attributed to the fact, that dissipation occurs in the  $\text{Sb}_2\text{Te}_3$  NR link. With increasing temperature the peaks shift toward zero bias in accordance with the decrease of  $\Delta$  with temperature. At the lower bias voltage side of the peak position,  $dV/dI$  decreases with decreasing the bias voltage due to the onset of Andreev reflection contributions.<sup>[51,52]</sup> The relatively small decrease in  $dV/dI$  compared to the higher bias side beyond the peak may be attributed to the presence of an interface barrier.<sup>[53,54]</sup> A finite excess current  $I_{\text{exc}} = I(eV/\Delta \gg 1) - V/R_N$  of 155 nA is extracted by a linear fitting of the  $I$ - $V$  curve at the normal state in the voltage range above 3.5 mV (Figure S2, Supporting Information). Note that  $R_N$  includes not only the interface resistance but also the resistance of the TI bridge, so that the actual value of  $I_{\text{exc}}$  might be somewhat smaller. At  $T = 0.5$  K we obtain  $eI_{\text{exc}}R_N/\Delta \approx 0.07$  based on the superconducting energy gap ( $\Delta \approx 1.4$  meV) and the normal state resistance ( $R_N \approx 650 \Omega$ ) of the Nb/ $\text{Sb}_2\text{Te}_3$ -NR/Nb junction. The barrier strength parameter  $Z$  according to the Octavio-Tinkham-Blonder-Klapwijk (OTBK) model<sup>[51,52]</sup> was obtained by using the analytical formula derived by Niebler et al.<sup>[55]</sup> We obtained a relatively large value of  $Z = 1$ , which might be caused by an inhomogeneous superconductor/topological insulator interface.

Let us return to the temperature dependence of  $dV/dI$  in the small bias current range which is plotted in Figure 2d. At a temperature of 0.5 K and close to zero bias current, the value of the differential resistance is basically zero, which we attribute to a Josephson supercurrent. As the bias current increases, the superconducting state is suppressed at  $I_{c1} \approx 0.15 \mu\text{A}$ . Upon increasing the temperature it is found that the superconducting state vanishes at about 2.5 K. At lower temperature a clear plateau is

observed, while at higher temperatures the transition is connected to a step feature at the dip shoulders in  $dV/dI$ . The peak feature assigned to  $I_{c2}$  at  $\pm 0.38 \mu\text{A}$  at 0.5 K is shifted to smaller bias current when the temperature is increased and eventually shrinks to a resistance step. This feature also vanishes at 2.5 K. In the following we have a closer look on the temperature dependence of  $I_{c1}$ . The second transition corresponding to  $I_{c2}$  follows the same trend and is not considered in more detail further on. Unfortunately, the two-critical-current phenomenon, as found here, was not observed in the four-terminal configuration of Nb/Cu/Nb junctions, so no direct comparison with that kind of junction is possible.<sup>[46]</sup>

In Figure 2f, the normalized critical currents  $I_{c1}/I_{c1}(0)$  is plotted as a function of temperature. We compared our results to theoretical models of superconductor/normal metal/superconductor (SNS) junctions. Regarding the model developed by Dubos et al.<sup>[56]</sup> for ideal junctions with no interface barriers we did not succeed to obtain a satisfying fit. We attribute this to the small  $eI_{c1}R_N = 69 \mu\text{eV}$  product, which would imply an unreasonably small value for the Thouless energy  $E_{\text{Th}} = \hbar D/L_{\text{in}}^2$ , with  $D$  the diffusion constant. However, as argued by Hammer et al.,<sup>[57]</sup> by introducing an effective Thouless energy  $E_{\text{Th}}^*$  being smaller than  $E_{\text{Th}}$  it is possible to include the contribution of an interface barrier. By applying this model it turned out that the drop of  $I_{c1}/I_{c1}(0)$  with temperature could not be reproduced. Probably the situation in our junction with a topological insulator bridge is more intrigue because of the presence of a topological surface channel and bulk carriers so that the available models for SNS junctions cannot be applied.

### 2.3. Magnetic Field Dependence of Superconductivity in Nb/ $\text{Sb}_2\text{Te}_3$ -NR/Nb Junctions

Figure 3a and Figures S3 and S4, Supporting Information, depict the evolution of  $I$ - $V$  and corresponding  $dV/dI$  characteristics of the Nb/ $\text{Sb}_2\text{Te}_3$ -NR/Nb nanodevice in an external magnetic field ( $B_{\perp}$ ) applied perpendicular to the junction plane at a temperature of 0.5 K. The fact, that no reemergence of the superconductivity is found upon increasing the magnetic field, as expected from a Fraunhofer-like pattern of the critical current, can be attributed to the very small effective junction area.<sup>[48,58,59]</sup> Here, the magnetic field acts a pair-breaking factor. With the junction area given by  $90 \text{ nm} \times 75 \text{ nm}$  we estimated a field of 0.3 T corresponding to a flux quantum penetrating the junction. In our case the superconducting range is beyond that value, which is in accordance with theory.<sup>[58]</sup> As the bias current increases, the valley at zero magnetic field broadens and disappears, that is, the supercurrent in the Nb/ $\text{Sb}_2\text{Te}_3$ -NR/Nb junction is suppressed. Then a peak at around  $0.4 \mu\text{A}$ , which related to  $I_{c2}$  (cf. Figure 2b), shifts toward lower bias current and eventually vanishes at around 5 T. Finally, the differential resistance is basically constant beyond 5 T, that is, the sample is in the normal state.

In the following we limit ourselves to the features around  $I_{c1}$ , since these are connected to the actual Josephson junction. As depicted in Figure 3b, one finds that the critical current  $I_{c1}$  of the Nb/ $\text{Sb}_2\text{Te}_3$ -NR/Nb junction basically decreases monotonously with the magnetic field. As mentioned before, we attribute the



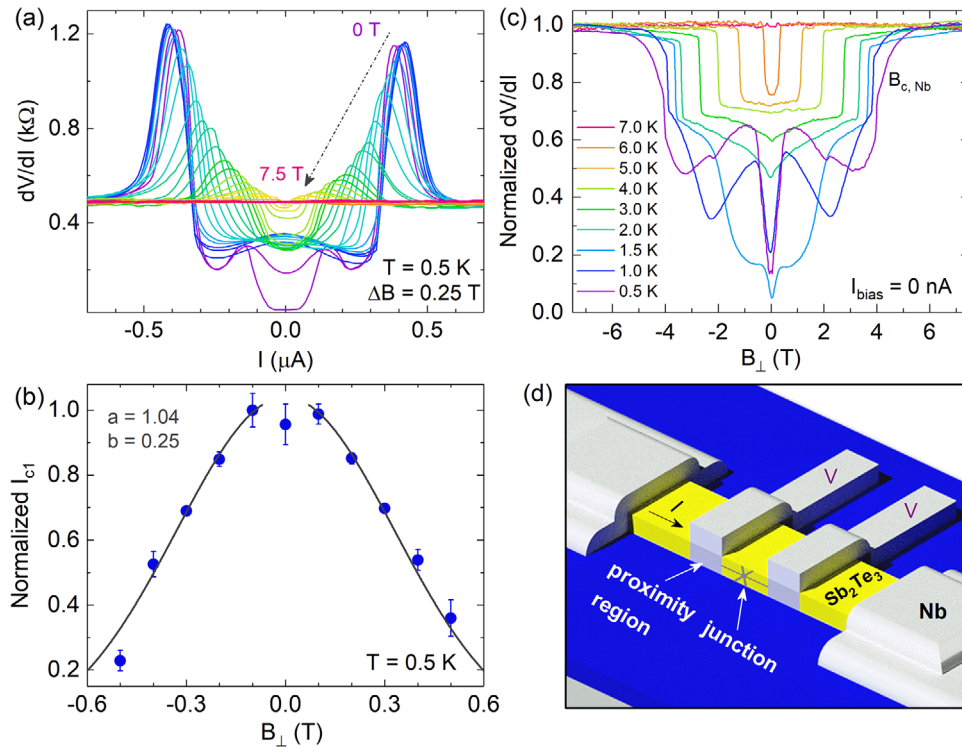


**Figure 3.** (Color online) a) Magnetic field dependency of  $dV/dI$  vs.  $I_{\text{bias}}$  at a temperature of 0.5 K. b) Normalized experimental (dot lines) and corresponding fitted (solid lines) critical currents  $I_{c1}$  as a function of magnetic field. The normalization is with respect to the maximum value of  $I_{c1}$ . c) Normalized  $dV/dI$  curves versus magnetic field during the cooling process from 7.0 to 0.5 K. d) A possible physical mechanism for the observed effects.

monotonous decrease to the small junction dimensions.<sup>[48,58,59]</sup> The decay of  $I_{c1}$  can be described by a Gaussian function<sup>[48]</sup>:  $I_{c1}(B) = I_{c1}(0) \cdot a e^{-b(BS/\Phi_0)^2}$ . Here,  $I_{c1}(0)$  is the critical current at zero magnetic field. The parameters  $a$  and  $b$  are constants,  $S$  is the effective area of the Nb/Sb<sub>2</sub>Te<sub>3</sub>-NR/Nb junction perpendicular to magnetic field.  $\Phi_0 = h/2e$  is the magnetic flux quantum. The coefficient  $b$  is 0.25 at 0.5 K being close to the value reported by Angers et al.<sup>[48]</sup> The value of  $b$  is found to decrease as the temperature increases. Around zero magnetic field we found indications of a reentrant behavior, that is,  $I_{c1}$  first increases when a magnetic field is applied. This is the reason, why the coefficient  $a = 1.04$  deviates slightly from one. Although we do not go into details about that feature, possible origins are phase breaking of Cooper pairs due to spin flip scattering, phase fluctuations, or improved thermalization in the superconducting leads due to the creation of vortices.<sup>[48,60–62]</sup>

In Figure 3c the differential resistance is plotted as a function of  $B_{\perp}$  for temperatures between 0.5 and 7.0 K. Beginning at 7.0 K  $dV/dI$  is constant without any features. At the next higher temperature of 6.0 K a narrow valley around zero magnetic field is observed, which can be related to the superconducting transition of the Nb electrodes ( $T_{c,\text{Nb}}$ ). As the temperature decreases further, the width of the valley, which directly corresponds to the critical field  $B_{c,\text{Nb}}(T)$  of the Nb electrodes broadens. Finally, at sufficiently low temperature, the step remains at  $B_{c,\text{Nb}} \approx 4$  T. The temperature dependence of  $B_{c,\text{Nb}}(T)$  can be fitted well to the common relationship for BCS superconductors:  $B_c(T) = B_c(0) \cdot [1 - (T/T_c)^2]$ , with  $B_{c,\text{Nb}}(0) = 3.9$  T, and  $T_{c,\text{Nb}} = 6.1$  K. At temperatures below 3.0 K, a dip closed to zero magnetic field appears and becomes

successively deeper. This feature is related to the superconducting transition of the Nb/Sb<sub>2</sub>Te<sub>3</sub>-NR/Nb junction. Its width is basically insensitive to temperature.

Finally, we will interpret the evolution of the superconducting transitions in our Nb/Sb<sub>2</sub>Te<sub>3</sub>-NR/Nb junctions based on the bias current, temperature, and magnetic field dependencies of the  $I$ - $V$  characteristics and the  $dV/dI$  traces. The first superconducting transition can be explained in the framework of a proximity induced weak-link Josephson junction (cf. Figure 3d). The missing appearance of the Fraunhofer-pattern of the magnetic field dependence of the critical current can be naturally explained by the very small junction dimensions.<sup>[48,58,59]</sup> Most likely, the Nb/Sb<sub>2</sub>Te<sub>3</sub>-NR/Nb junction is formed by a proximity induced superconducting state in the Sb<sub>2</sub>Te<sub>3</sub> nanoribbon right underneath the inner Nb electrodes which are connected by the few tens of nanometers short Sb<sub>2</sub>Te<sub>3</sub> bridge. What is more intriguing is the second transition, which is somehow directly related to the superconducting state of the Nb electrodes. Since we performed our experiment in a four-terminal configuration, the current in the junction is fed from the outer contacts through the nanoribbon, that is, in first approximation it will not pass through the inner Nb contact. Presumably, the second transition connected to  $I_{c2}$  can be related to the proximity induced area in the Sb<sub>2</sub>Te<sub>3</sub> nanoribbon underneath the inner electrodes. Owing to the strong proximity effect because of the small thickness of the Sb<sub>2</sub>Te<sub>3</sub> nanoribbon, the critical magnetic field and the critical temperature are comparable to the one of the metallic Nb electrodes. The assumption of proximity induced regions in the nanoribbon is supported by the relatively small critical current  $I_{c2}$  of only  $0.38 \mu\text{A}$  at 0.4 K.

In case that the bias current would mainly take a path through the inner Nb electrodes bypassing the  $\text{Sb}_2\text{Te}_3$  nanoribbon underneath a larger critical current would be expected. However, we cannot exclude that the bias current splits up and a fraction flows through the Nb electrodes.

### 3. Conclusion

In summary, we have explored and experimentally validated the evolution of proximity induced superconductivity in Nb/ $\text{Sb}_2\text{Te}_3$ -nanoribbon/Nb junctions based on the temperature and magnetic field dependent measurements of  $dV/dI$  and  $I$ - $V$  curves. At a temperature of 0.5 K, we observed a critical supercurrent  $I_{c1}$  of 0.15  $\mu\text{A}$  which we attribute to a proximity induced Josephson weak link junction. Furthermore, a second transition  $I_{c2}$  is found at 0.38  $\mu\text{A}$ , which probably is due to the proximity induced superconducting areas in the  $\text{Sb}_2\text{Te}_3$  located directly underneath the Nb electrodes. The temperature dependence of  $I_{c1}$  can be explained in the framework of a diffusive junction. However, some deviations from the ideal behavior is observed, which we attribute to the presence of a topological surface channel and bulk carriers. In addition, interface effects might also play a role. By applying a perpendicular magnetic field, a monotonous decrease of the critical current is observed. This is explained by the small junction dimensions, where the magnetic field acts as a pair-breaking factor.

By the results presented here we could show that our Nb/ $\text{Sb}_2\text{Te}_3$ -nanoribbon/Nb junctions are promising candidates for realizing topological quantum circuits based on Majorana zero mode. As a next step to that goal it would be interesting to study the behavior of the junction, when an axially oriented magnetic field is applied. In this case, the flux encircled by the topological surface states results in a modulation of the quantized energy levels in the nanoribbon and by that in an according modulation of the supercurrent. In fact, for creating Majorana zero modes biasing to  $\Phi_0$  is required.<sup>[31]</sup>

### 4. Experimental Section

**$\text{Sb}_2\text{Te}_3$  Nanoribbon Synthesis:**  $\text{Sb}_2\text{Te}_3$  nanoribbons were grown by a Au-catalyzed chemical vapor deposition (CVD) method. First, the Si/ $\text{SiO}_2$  substrates were treated with acetone, iso-propyl alcohol, and deionized water in an ultrasonic cleaning bath and subsequently in a piranha solution ( $\text{H}_2\text{SO}_4$ :30%  $\text{H}_2\text{O}_2 = 3 : 1$ ) at about 100 °C for 15 min to remove organic residue. Second, the substrates were washed in deionized water, dried with high-purity nitrogen, and then immersed in a Au nanoparticles solution for 2 min and rinsed with deionized water. Finally, Sb powder was placed at the heating zone of a quartz tube furnace. Te powder was located at 13.5 cm upstream from the Sb powder. The Si/ $\text{SiO}_2$  substrates covered with Au nanoparticles were put in the downstream 10.5 cm away from the Sb powder. Subsequently, the furnace was evacuated and flushed three times with Ar gas before heating to 430 °C and persist for 6 h. During this program, the Ar flow rate and the pressure in the quartz tube were about 80 sccm and 10 torr, respectively.

**$\text{Sb}_2\text{Te}_3$ -Based Nanodevice Fabrication:** In order to contact a single  $\text{Sb}_2\text{Te}_3$  NR with Nb electrodes, the as-grown nanoribbons were transferred to a Si/ $\text{SiO}_2$ / $\text{Si}_3\text{N}_4$  substrate with predefined markers for electron beam lithography. A two-layer (copolymer/950 K) polymethyl methacrylate (PMMA) resist was adopted to define the shape of the Nb leads. In order to obtain a transparent interface between the superconducting Nb and  $\text{Sb}_2\text{Te}_3$ , the samples were exposed to an oxygen plasma to remove PMMA

residues in the contact area. Before the deposition of the 60-nm-thick Nb electrodes by magnetron sputtering, the samples were gently cleaned by  $\text{Ar}^+$  plasma milling to remove the native oxide layer on the  $\text{Sb}_2\text{Te}_3$  surface.

**Crystalline Structure, Superconductivity, and Magnetotransport Characterizations:** The crystalline structure of the  $\text{Sb}_2\text{Te}_3$  NRs has been investigated by HRTEM, XRD, and Raman scattering. Furthermore, temperature and magnetic field dependent  $I$ - $V$  and  $dV/dI$  characteristics were measured using standard lock-in technique in a  $^3\text{He}$  cryostat with a temperature of 0.5 K and a magnetic field ranging from  $-8$  to  $8$  T. A four-terminal current-driven geometry was performed to directly measure the voltage drop across the section of TI between the nearest internal Nb electrodes. The external pair of electrodes is used to drive a DC + AC current ( $I = I_{\text{bias}} + I_{\text{AC}}$ ), while the internal pair is used to probe the potential differences of the TI section between the internal Nb leads. The frequency and amplitude of the alternating current are 77 Hz and 40 nA, respectively. Note that the applied bias current should be as small as possible to avoid electron heating and damage of devices. For consistency reasons we present the data of a single representative sample. Multiple samples were measured, all showed a similar behavior as the one discussed in the manuscript.

### Supporting Information

Supporting Information is available from the Wiley Online Library or from the author.

### Acknowledgements

J.Z. and A.R.J. contributed equally to this work. The authors thank Herbert Kertz, Stefan Trellenkamp, Yulieth C. Arango, Tobias Schmitt, and Michael Schleenvoigt for discussions, and the Helmholtz Nano Facility (HNF) for help with devices fabrication in its clean room facilities. This work was financially supported by the International Postdoctoral Exchange Fellowship Program (No.20161008), the German Deutsche Forschungsgemeinschaft (DFG) under the priority program SPP1666 "Topological Insulators," the Helmholtz Association the "Virtual Institute for Topological Insulators" (VITI), by the Deutsche Forschungsgemeinschaft (DFG, German Research Foundation) under Germany's Excellence Strategy - Cluster of Excellence Matter and Light for Quantum Computing (ML4Q) EXC 2004/1 - 390 534 769, the National Natural Science Foundation of China (Grant No. 61504156), the National Key R&D Program of China (Grants No. 2017YFA0303403 and No. 2018YFB0406500), and the Projects of Science and Technology Commission of Shanghai Municipality (Grant No. 18JC1412400, 19ZR1473400).

### Conflict of Interest

The authors declare no conflict of interest.

### Keywords

proximity effect,  $\text{Sb}_2\text{Te}_3$  nanoribbons, superconductivity, topological insulators

Received: May 29, 2020  
Published online: July 9, 2020

[1] H. Zhang, C.-X. Liu, X.-L. Qi, X. Dai, Z. Fang, S.-C. Zhang, *Nat. Phys.* **2009**, 5, 438.

- [2] D. O. Scanlon, P. D. C. King, R. P. Singh, A. de la Torre, S. M. Walker, G. Balakrishnan, F. Baumberger, C. R. A. Catlow, *Adv. Mater.* **2012**, 24, 2154.
- [3] Y. Ando, *J. Phys. Soc. Jpn.* **2013**, 82, 102001.
- [4] M. Z. Hasan, C. L. Kane, *Rev. Mod. Phys.* **2010**, 82, 3045.
- [5] X.-L. Qi, S.-C. Zhang, *Rev. Mod. Phys.* **2011**, 83, 1057.
- [6] X. Wang, L. Cheng, D. Zhu, Y. Wu, M. Chen, Y. Wang, D. Zhao, C. B. Boothroyd, Y. M. Lam, J.-X. Zhu, M. Battiato, J. C. W. Song, H. Yang, E. E. M. Chia, *Adv. Mater.* **2018**, 30, 1802356.
- [7] K. Moors, P. Schüffegen, D. Rosenbach, T. Schmitt, T. Schäpers, T. L. Schmidt, *Phys. Rev. B* **2018**, 97, 245429.
- [8] I. A. Nechaev, I. Aguilera, V. De Renzi, A. di Bona, A. Lodi Rizzini, A. M. Mio, G. Nicotra, A. Politano, S. Scalese, Z. S. Aliev, M. B. Babanly, C. Friedrich, S. Blügel, E. V. Chulkov, *Phys. Rev. B* **2015**, 91, 245123.
- [9] J. L. Zhang, S. J. Zhang, H. M. Weng, W. Zhang, L. X. Yang, Q. Q. Liu, S. M. Feng, X. C. Wang, R. C. Yu, L. Z. Cao, L. Wang, W. G. Yang, H. Z. Liu, W. Y. Zhao, S. C. Zhang, X. Dai, Z. Fang, C. Q. Jin, *Proc. Natl. Acad. Sci.* **2011**, 108, 24.
- [10] M. Veldhorst, M. Snelder, M. Hoek, T. Gang, V. K. Guduru, X. L. Wang, U. Zeitler, W. G. van der Wiel, A. A. Golubov, H. Hilgenkamp, A. Brinkman, *Nat. Mater.* **2012**, 11, 417.
- [11] F. Qu, F. Yang, J. Shen, Y. Ding, J. Chen, Z. Ji, G. Liu, J. Fan, X. Jing, C. Yang, L. Lu, *Sci. Rep.* **2012**, 2, 339.
- [12] S. Cho, B. Dellabetta, A. Yang, J. Schneeloch, Z. Xu, T. Valla, G. Gu, M. J. Gilbert, N. Mason, *Nat. Commun.* **2013**, 4, 1689.
- [13] M. Snelder, C. G. Molenaar, Y. Pan, D. Wu, Y. K. Huang, A. de Visser, A. A. Golubov, W. G. van der Wiel, H. Hilgenkamp, M. S. Golden, A. Brinkman, *Supercond. Sci. Technol.* **2014**, 27, 104001.
- [14] L. Galletti, S. Charpentier, M. Iavarone, P. Lucignano, D. Massarotti, R. Arpaia, Y. Suzuki, K. Kadowaki, T. Bauch, A. Tagliacozzo, F. Tafuri, F. Lombardi, *Phys. Rev. B* **2014**, 89, 134512.
- [15] S. Ghatak, O. Breunig, F. Yang, Z. Wang, A. A. Taskin, Y. Ando, *Nano Lett.* **2018**, 18, 5124.
- [16] P. Schüffegen, D. Rosenbach, C. Li, T. W. Schmitt, M. Schleenvoigt, A. R. Jalil, S. Schmitt, J. Kölzer, M. Wang, B. Bennemann, U. Parlak, L. Kibkalo, S. Trellenkamp, T. Grap, D. Meertens, M. Luysberg, G. Mussler, E. Berenschoot, N. Tas, A. A. Golubov, A. Brinkman, T. Schäpers, D. Grützmacher, *Nat. Nanotechnol.* **2019**.
- [17] P. Zareapour, A. Hayat, S. Y. F. Zhao, M. Kreshchuk, A. Jain, D. C. Kwok, N. Lee, S.-W. Cheong, Z. Xu, A. Yang, G. D. Gu, S. Jia, R. J. Cava, K. S. Burch, *Nat. Commun.* **2012**, 3, 1.
- [18] M. Chen, X. Chen, H. Yang, Z. Du, H.-H. Wen, *Sci. Adv.* **2018**, 4, eaat1084.
- [19] L. Fu, C. L. Kane, *Phys. Rev. Lett.* **2008**, 100, 096407.
- [20] A. Cook, M. Franz, *Phys. Rev. B* **2011**, 84, 201105.
- [21] A. M. Cook, M. M. Vazifeh, M. Franz, *Phys. Rev. B* **2012**, 86, 155431.
- [22] G.-Y. Huang, H. Q. Xu, *Phys. Rev. B* **2017**, 95, 155420.
- [23] A. Kitaev, *Ann. Phys.* **2003**, 303, 2.
- [24] J. Alicea, *Rep. Prog. Phys.* **2012**, 75, 076501.
- [25] J. Wiedenmann, E. Bocquillon, R. S. Deacon, S. Hartinger, O. Herrmann, T. M. Klapwijk, L. Maier, C. Ames, C. Brüne, C. Gould, A. Oiwa, K. Ishibashi, S. Tarucha, H. Buhmann, L. W. Molenkamp, *Nat. Commun.* **2016**, 7, 10303.
- [26] E. Bocquillon, R. S. Deacon, J. Wiedenmann, P. Leubner, T. M. Klapwijk, C. Brüne, K. Ishibashi, H. Buhmann, L. W. Molenkamp, *Nat. Nanotechnol.* **2017**, 12, 137.
- [27] C. Li, J. C. de Boer, B. de Ronde, S. V. Ramankutty, E. van Heumen, Y. Huang, A. de Visser, A. A. Golubov, M. S. Golden, A. Brinkman, *Nat. Mater.* **2018**, 17, 875.
- [28] P. Lošt'ák, Z. Starý, J. Horák, J. Pánčíř, *Phys. Status Solidi (a)* **1989**, 115, 87.
- [29] C. Weyrich, T. Merzenich, J. Kampmeier, I. E. Batov, G. Mussler, J. Schubert, D. Grützmacher, T. Schäpers, *Appl. Phys. Lett.* **2017**, 110, 092104.
- [30] M. Eschbach, E. Mlynczak, J. Kellner, J. Kampmeier, M. Lanius, E. Neumann, C. Weyrich, M. Gehlmann, P. Gospodaric, S. Döring, G. Mussler, N. Demarina, M. Luysberg, G. Bihlmayer, T. Schäpers, L. Plucinski, S. Blügel, M. Morgenstern, C. M. Schneider, D. Grützmacher, *Nat. Commun.* **2015**, 6, 8816.
- [31] J. H. Bardarson, P. W. Brouwer, J. E. Moore, *Phys. Rev. Lett.* **2010**, 105, 156803.
- [32] J. H. Bardarson, J. E. Moore, *Rep. Prog. Phys.* **2013**, 76, 056501.
- [33] F. Xiu, L. H. Wang, L. Cheng, L.-T. Chang, M. Lang, G. Huang, X. Kou, Y. Zhou, X. Jiang, Z. Chen, J. Zou, A. Shailos, K. L. Wang, *Nat. Nanotechnol.* **2011**, 6, 216.
- [34] J. Dufouleur, L. Veyrat, A. Teichgräber, S. Neuhaus, C. Nowka, S. Hampel, J. Cayssol, J. Schumann, B. Eichler, O. G. Schmidt, B. Büchner, R. Giraud, *Phys. Rev. Lett.* **2013**, 110, 186806.
- [35] S. S. Hong, Y. Zhang, J. J. Cha, X.-L. Qi, Y. Cui, *Nano Lett.* **2014**, 14, 2815.
- [36] S. Cho, B. Dellabetta, R. Zhong, J. Schneeloch, T. Liu, G. Gu, M. J. Gilbert, N. Mason, *Nat. Commun.* **2015**, 6, <https://doi.org/10.1038/ncomms8634>.
- [37] L. A. Jauregui, M. T. Pettes, L. P. Rokhinson, L. Shi, Y. P. Chen, *Nat. Nanotechnol.* **2016**, 11, 345.
- [38] Y. C. Arango, L. Huang, C. Chen, J. Avila, M. C. Asensio, D. Grützmacher, H. Lüth, J. G. Lu, T. Schäpers, *Sci. Rep.* **2016**, 6, 29493.
- [39] J. S. Lee, S. Brittman, D. Yu, H. Park, *J. Am. Chem. Soc.* **2008**, 130, 6252.
- [40] G. Sosso, S. Caravati, M. Bernasconi, *J. Phys.: Condens. Matter* **2009**, 21, 095410.
- [41] R. He, Z. Wang, R. L. J. Qiu, C. Delaney, B. Beck, T. E. Kidd, C. C. Chancey, X. P. A. Gao, *Nanotechnology* **2012**, 23, 455703.
- [42] D. Bessas, I. Sergueev, H.-C. Wille, J. Perßon, D. Ebling, R. P. Hermann, *Phys. Rev. B* **2012**, 86, 224301.
- [43] D. Teweldebrhan, V. Goyal, A. A. Balandin, *Nano Lett.* **2010**, 10, 1209.
- [44] C. Wang, X. Zhu, L. Nilsson, J. Wen, G. Wang, X. Shan, Q. Zhang, S. Zhang, J. Jia, Q. Xue, *Nano Research* **2013**, 6, 688.
- [45] H. Courtois, P. Gandit, B. Pannetier, *Phys. Rev. B* **1995**, 52, 1162.
- [46] O. V. Skryabina, S. V. Egorov, A. S. Goncharova, A. A. Klimenko, S. N. Kozlov, V. V. Ryazanov, S. V. Bakurskiy, M. Y. Kupriyanov, A. A. Golubov, K. S. Napol'skii, V. S. Stolyarov, *Appl. Phys. Lett.* **2017**, 110, 222605.
- [47] J. P. Carbotte, *Rev. Mod. Phys.* **1990**, 62, 1027.
- [48] L. Angers, F. Chiodi, G. Montambaux, M. Ferrier, S. Guéron, H. Bouchiat, J. C. Cuevas, *Phys. Rev. B (Condensed Matter and Materials Physics)* **2008**, 77, 165408.
- [49] B.-K. Kim, H.-S. Kim, Y. Yang, X. Peng, D. Yu, Y.-J. Doh, *ACS nano* **2017**, 11, 221.
- [50] G. E. Blonder, M. Tinkham, T. M. Klapwijk, *Phys. Rev. B* **1982**, 25, 4515.
- [51] M. Octavio, M. Tinkham, G. E. Blonder, T. M. Klapwijk, *Phys. Rev. B* **1983**, 27, 6739.
- [52] K. Flensberg, J. B. Hansen, M. Octavio, *Phys. Rev. B* **1988**, 38, 8707.
- [53] J. C. Cuevas, J. Hammer, J. Kopu, J. K. Viljas, M. Eschrig, *Phys. Rev. B* **2006**, 73, 184505.
- [54] R. Frielinghaus, I. E. Batov, M. Weides, H. Kohlstedt, R. Calarco, T. Schäpers, *Appl. Phys. Lett.* **2010**, 96, 132504.
- [55] G. Niebler, G. Cuniberti, T. Novotny, *Supercond. Sci. Technol.* **2009**, 22, 085016.
- [56] P. Dubos, H. Courtois, B. Pannetier, F. K. Wilhelm, A. D. Zaikin, G. Schön, *Phys. Rev. B* **2001**, 63, 064502.

- [57] J. C. Hammer, J. C. Cuevas, F. S. Bergeret, W. Belzig, *Phys. Rev. B (Condensed Matter and Materials Physics)* **2007**, 76, 064514.
- [58] J. C. Cuevas, F. S. Bergeret, *Phys. Rev. Lett.* **2007**, 99, 217002.
- [59] H. Y. Günel, I. E. Batov, H. Hardtdegen, K. Sladek, A. Winden, K. Weis, G. Panaitov, D. Grützmacher, T. Schäpers, *J. Appl. Phys.* **2012**, 112, 034316.
- [60] A. Rogachev, T.-C. Wei, D. Pekker, A. T. Bollinger, P. M. Goldbart, A. Bezryadin, *Phys. Rev. Lett.* **2006**, 97, 137001.
- [61] P. Xiong, A. V. Herzog, R. C. Dynes, *Phys. Rev. Lett.* **1997**, 78, 927.
- [62] J. T. Peltonen, J. T. Muhonen, M. Meschke, N. B. Kopnin, J. P. Pekola, *Phys. Rev. B* **2011**, 84, 220502.